

¹ pyTopoComplexity: A Python package for topographic complexity analysis

³ **Larry Syu-Heng Lai**  ^{1¶}, **Adam M. Booth**  ², **Alison R. Duvall**  ¹, and **Erich Herzog**  ¹

⁵ 1 Department of Earth and Space Sciences, University of Washington, Seattle, Washington, USA

⁶ 2 Department of Geology, Portland State University, Portland, Oregon, USA ¶ Corresponding author

DOI: [10.xxxxxx/draft](https://doi.org/10.xxxxxx/draft)

Software

- ⁷ ▪ [Review](#) 
- ⁸ ▪ [Repository](#) 
- ⁹ ▪ [Archive](#) 

Editor: 

Submitted: 30 August 2024

Published: unpublished

License

Authors of papers retain copyright and release the work under a Creative Commons Attribution 4.0 International License ([CC BY 4.0](https://creativecommons.org/licenses/by/4.0/))

Summary

¹⁰ **pyTopoComplexity** is a Python package that provides a computationally efficient and customizable implementation of four modern methods for quantifying topographic complexity. These methods include two-dimensional continuous wavelet transform analysis, fractal dimension estimation, Rugosity Index and Terrain Position Index calculations across various spatial scales. ¹¹ This package addresses the scarcity of open-source software for these sophisticated methods needed in modern terrain analysis, and facilitates data comparison and reproducibility. In ¹² the [software repository](#), we also include a Jupyter Notebook file that integrates components from the Python-based surface-process modeling platform **Landlab** ([Hobley et al., 2017](#)). The ¹³ notebook allows researchers to simulate the smoothing of topography over time through terrestrial nonlinear hillslope diffusion processes. By combining these features, **pyTopoComplexity** ¹⁴ advances the toolset available to researchers for measuring and simulating the time-dependent ¹⁵ persistence of topographic complexity signatures against environmental forces on terrain ¹⁶ surfaces.

Statement of need

²² Topographic complexity, often referred to as topographic roughness or surface roughness, ²³ provides critical insights into surface processes and the interactions among the geosphere, ²⁴ biosphere, and hydrosphere ([Dietrich & Perron, 2006](#)). With the increasing availability, utility, ²⁵ and popularity of digital terrain model (DTM) data, quantifying topographic complexity has ²⁶ become an essential step in terrain analysis across various research fields. This necessity ²⁷ spans applications such as terrain classification and mapping at various spatial scales ([John B. ²⁸ Lindsay et al., 2019](#); [Pardo-Igúzquiza & Dowd, 2022a](#); [Robbins, 2018](#); [Weiss, 2001](#)), evaluating ²⁹ the depositional age of event sedimentation (e.g., landslides, avulsion on alluvial fans) and ³⁰ subsequent erosion processes ([Booth et al., 2017](#); [Herzig et al., 2023](#); [Hetz et al., 2016](#); ³¹ [Johnstone et al., 2018](#); [LaHusen et al., 2020](#)), and identifying habitats to assess ecological ³² diversity on land and seafloor ([Frost et al., 2005](#); [Hetz et al., 2016](#); [Wilson et al., 2007](#)).

³³ In recent years, several advanced methods for quantifying topographic complexity have been ³⁴ developed, including two-dimensional continuous wavelet transform (2D-CWT) analysis ([Berti ³⁵ et al., 2013](#); [Booth et al., 2009](#)), fractal dimension estimation ([Glenn et al., 2006](#); [Pardo-³⁶ Igúzquiza & Dowd, 2020](#); [Robbins, 2018](#); [Taud & Parrot, 2005](#)), and Rugosity Index calculation ³⁷ ([Du Preez, 2015](#); [Jenness, 2004](#)). These methods are considered more effective for topographic ³⁸ complexity analysis tasks compared to conventional morphological metrics such as variations ³⁹ in local slope and relief. Despite their importance, comprehensive publicly available tools that ⁴⁰ incorporate these advanced methods for studying topographic complexity are lacking. Common ⁴¹ open-source geospatial analysis software, such as QGIS ([QGIS Development Team, 2023](#)),

⁴² GRASS GIS ([GRASS Development Team, 2023](#)), and WhiteboxTools ([J. B. Lindsay, 2016](#)),
⁴³ only implement basic conventional methods, limiting the reproducibility and comparability of
⁴⁴ these newer approaches. Although specialized programs for calculating the Rugosity Index
⁴⁵ exist ([Benham, 2022](#); [Walbridge et al., 2018](#)), they have been confined to marine bathymetric
⁴⁶ studies and involve various mathematical limitations, assumptions, and designs.

⁴⁷ To address this gap, we have developed an open-source Python toolkit called **pyTopoComplexity**.
⁴⁸ This toolkit offers computationally efficient and easily customizable implementations for
⁴⁹ performing and visualizing the results of 2D-CWT, fractal dimension, and Rugosity Index
⁵⁰ calculations (see Table 1[Table 1](#)). Additionally, **pyTopoComplexity** includes a module for
⁵¹ calculating the Terrain Position Index, a widely used metric in geomorphology research
⁵² ([Deumlich et al., 2010](#); [Liu et al., 2011](#); [Newman et al., 2018](#)) and often used alongside
⁵³ Rugosity Index in marine geological and ecological studies ([Walbridge et al., 2018](#); [Wilson et](#)
⁵⁴ [al., 2007](#)).

Table 1: Table 1 : Modules contained in the **pyTopoComplexity** package.

Modules	Classes	Method Descriptions	References
pycwtmexhat.py	CWTMexHat	Quantifies the wavelet-based curvature of the land surface using two-dimensional continuous wavelet transform (2D-CWT) with a Mexican Hat wavelet	Booth et al. (2009) ; Booth et al. (2017)
pyfracd.py	FracD	Conducts fractal dimension analysis on the land surface using variogram procedures	Wen & Sinding-Larsen (1997) ; Pardo-Igúzquiza & Dowd (2020)
pyrugostiy.py	RugosityIndex	Calculates the Rugosity Index of the land surface	Jenness (2004) ; Du Preez (2015)
pytpi.py	TPI	Calculates Terrain Position Index of the land or seafloor surface	Weiss (2001) ; Walbridge et al. (2018)

⁵⁵ This toolkit detects the grid spacing and units of the projected coordinate system (acceptable
⁵⁶ in meters, U.S. survey feet, and international feet) from the input raster DTM file (GeoTIFF
⁵⁷ format) and automatically conducts unit conversions in necessary calculation steps to ensure
⁵⁸ data consistency and reproducibility. Removal of results at nodes affected by edge effects due
⁵⁹ to no-data values outside the input raster occurs by default. Users can define the suitable
⁶⁰ spatial scale to match their research purposes and choose computational approaches (e.g.,
⁶¹ chunk processing, faster mathematical approximations) to optimize performance (see details in
⁶² the **Methods and features overview** section).

⁶³ Each module of **pyTopoComplexity** includes a corresponding [example Jupyter Notebook file](#)
⁶⁴ with usage instructions. These examples utilize lidar DTM data (~1 m resolution) from the
⁶⁵ 2014 ‘Oso’ deep-seated landslide along the North Fork Stillaguamish River valley in Washington
⁶⁶ State, USA ([Washington Geological Survey, 2023](#)). In the software repository, we also include
⁶⁷ an additional Jupyter Notebook file [nonlineardiff_Landlab.ipynb](#), which allows researchers to
⁶⁸ simulate the smoothing of topography over time via terrestrial nonlinear hillslope diffusion

69 processes (Roering et al., 1999). This is achieved by employing the TaylorNonLinearDiffuser
 70 module from the terrainBento Python package (Barnhart et al., 2019) and running the
 71 simulation in the Landlab environment (Hobley et al., 2017).

72 By bridging the gap between different advanced terrain analytical approaches and incorporating
 73 functionality for landscape evolution modeling, **pyTopoComplexity** serves as a valuable
 74 resource for topographic complexity research and has the potential to foster new insights and
 75 interdisciplinary collaborations in the fields of geology, geomorphology, geography, ecology, and
 76 oceanography.

77 Methods and features overview

78 Two-dimensional continuous wavelet transform analysis

79 The **pycwtmexhat.py** module in **pyTopoComplexity** implements the 2D-CWT method for
 80 terrain analysis, providing detailed information on how amplitude is distributed across spatial
 81 frequencies at each position in the data by transforming spatial data into position-frequency
 82 space. When used with the Gaussian family of wavelets, this method is particularly effective
 83 for depicting the Laplacian of topography (Lashermes et al., 2007; Torrence & Compo,
 84 1998), revealing concave and convex regions of topography at various smoothing-length scales
 85 (Malamud & Turcotte, 2001; Struble et al., 2021), identifying deep-seated landslides (Berti
 86 et al., 2013; Booth et al., 2009), and estimating the depositional ages of landslide deposits
 87 (Booth et al., 2017; Herzig et al., 2023; LaHusen et al., 2020; Underwood, 2022).

88 The 2D-CWT is computed by convolving the elevation data z with a wavelet family ψ , using a
 89 wavelet scale parameter s at every location (x, y) :

$$C(s, x, y) = \Delta^2 \int_{-\infty}^{\infty} \int_{-\infty}^{\infty} z(x, y) \psi(x, y) dx dy$$

90 , where the resultant wavelet coefficient $C(s, x, y)$ provides a measure of how well the wavelet
 91 ψ matches the data z at each grid point (Torrence & Compo, 1998). Unlike other techniques
 92 that use moving windows to detect regional topographic complexity, the 2D-CWT method
 93 stands out by isolating specific landform features at the scale of the designated wavelength
 94 while filtering out noise from terrain variations at longer or shorter wavelengths. When s is
 95 large, ψ is spread out, capturing long-wavelength features of z ; when s is small, ψ becomes
 96 more localized, making it sensitive to fine-scale features of z . In this implementation, we use
 97 the 2D Ricker or Marr wavelet (i.e., Mexican hat wavelet) function to define ψ (Ricker, 1943):

$$\psi = -\frac{1}{\pi(s\Delta)^4} \left(1 - \frac{x^2 + y^2}{2s^2}\right) e^{-\left(\frac{x^2+y^2}{2s^2}\right)} \quad \lambda = \frac{2\pi s}{\sqrt{5/2}} \Delta$$

98 The Mexican hat wavelet, as defined above, corresponds to the second derivative of a Gaussian
 99 envelope. Its Fourier wavelength (λ) depends on the chosen wavelet scale (s) and the grid
 100 spacing (Δ) of the input DTM raster. The wavelet function ψ is scaled based on the wavelet
 101 scale parameter s and the grid spacing Δ , ensuring that the resultant wavelet coefficient C
 102 represents concave and convex landforms according to the wavelet scale s . Users can specify
 103 the wavelength λ in meters as the target spatial scale for landform roughness analysis. The
 104 **pycwtmexhat.py** module will automatically compute the wavelet scale s based on the grid
 105 spacing (Δ) of the input raster file (Figure 1Figure 1). In this module, users can choose to
 106 perform convolution either in the original domain (i.e., direct convolution) or in the frequency
 107 domain (i.e., using the Fast Fourier Transform) with the `convolve2d` and `fftconvolve` functions
 108 from the **SciPy** package, respectively (Virtanen et al., 2020). By default, the module uses
 109 `fftconvolve` for greater computational efficiency.

We note that the equations for C and ψ presented here are mathematical approaches adapted in later publications (Herzig et al., 2023; LaHusen et al., 2020; Underwood, 2022) and ongoing works on landslide mapping and age dating studies (Booth & Pétursson, 2023; Lai et al., 2023; Ozioko et al., 2023). There are minor differences in the proportionality constant used to define ψ and the conventions used to present the magnitude of the wavelet coefficients C , compared to earlier similar research by Booth et al. (2009) and Booth et al. (2017) (original MATLAB codes available from [Booth's personal website](#)). These differences in mathematical approach will by definition result in C values in different units and order of magnitude (e.g., 10^{-3} to 10^{-4} [m^{-2}] in Booth et al. (2017) and prior studies; 10^{-2} to 10^{-3} [m^{-1}] in LaHusen et al. (2020) thereafter). Despite this discrepancy, the C values yielded from these two approaches are linearly scaled and interconvertible, and they both reflect identical spatiotemporal patterns of topographic complexity (i.e., surface roughness).

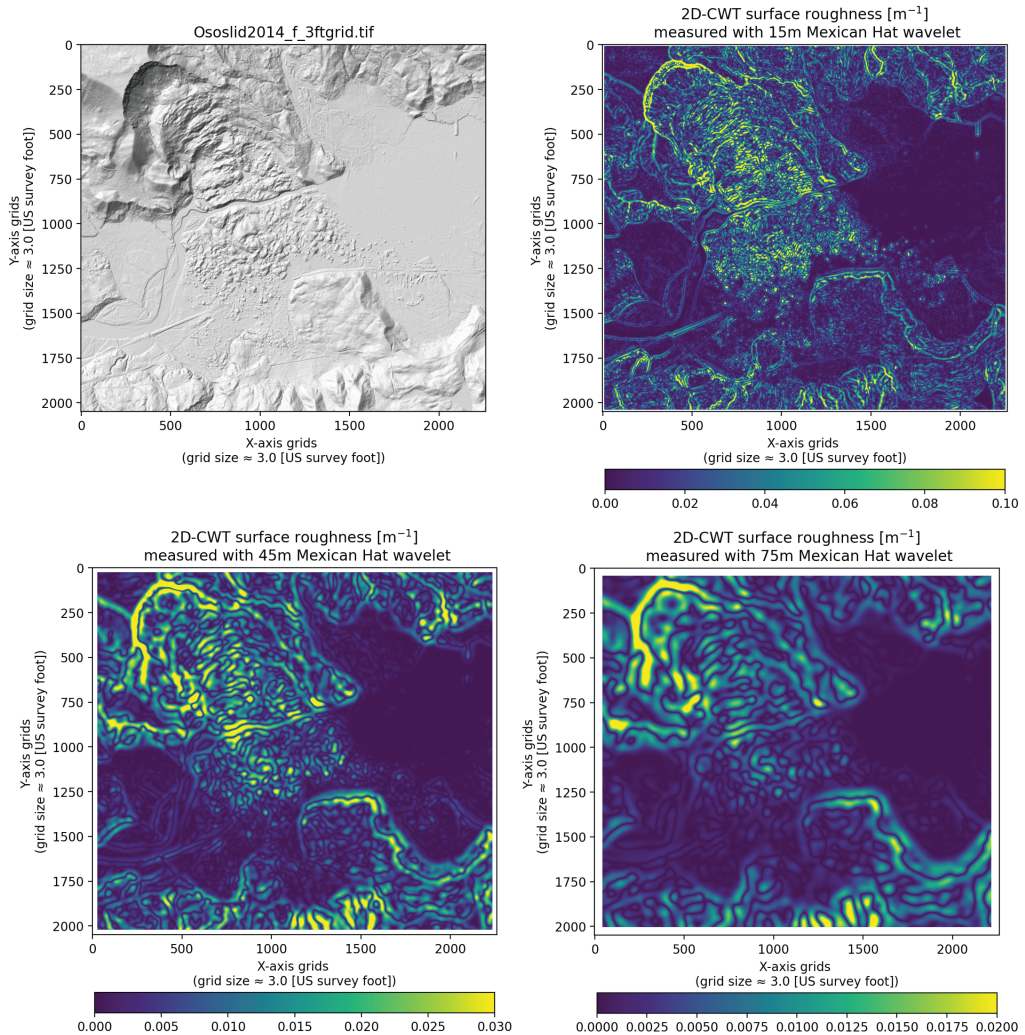


Figure 1: Figure 1. Hillshade map of the 2014 Oso Landslide region (upper-left) and the results of the two-dimensional continuous wavelet transform (2D-CWT) analysis using the `pycwtmexhat.py` module, with designated Fourier wavelengths (λ) of the Mexican Hat wavelet at 15 m, 45 m, and 75 m.

Fractal dimension analysis

The `pyfracd.py` module in `pyTopoComplexity` calculates the fractal dimension, which measures the fractal characteristics of natural features (Mandelbrot & Wheeler, 1983). This method

¹²⁵ provides insights into the self-similarity of landscapes, helping quantify their irregularity and
¹²⁶ fragmentation, which is crucial for studying the surface processes that shape Earth and planetary
¹²⁷ surfaces ([Xu et al., 1993](#)).

¹²⁸ In this module, we adapt the variogram method to estimate the local fractal dimension within
¹²⁹ a moving window centered at each cell of the DTM ([Pardo-Igúzquiza & Dowd, 2020, 2022a](#);
¹³⁰ [Taud & Parrot, 2005](#)). This approach simplifies the problem to estimating the fractal dimension
¹³¹ of one-dimensional topographic profiles ([Dubuc et al., 1989](#)) within a two-dimensional moving
¹³² window. For a one-dimensional profile of length L , the variogram $\gamma_1(k)$ can be estimated at
¹³³ the K lag distances (K lag distances ($k = 1, \dots, K$) by:

$$\gamma_1(k) = \frac{1}{2(L-k)} \sum_{l=1}^{L-k} [Z(i) - Z(i+l)]^2$$

¹³⁴ , where $Z(i)$ is the elevation at location i along the profile. The local fractal dimension (FD)
¹³⁵ is estimated from one-dimensional profiles in principal directions (i.e., horizontal, vertical, and
¹³⁶ diagonal) within a square moving window. Assuming that fractional Brownian motion is an
¹³⁷ appropriate stochastic model for natural surfaces, its variogram follows a power-law model
¹³⁸ with respect to k ([Wen & Sinding-Larsen, 1997](#)):

$$\gamma_1(k) = \alpha h^\beta, \quad \alpha \geq 0; \quad 0 \leq \beta < 2$$

¹³⁹ , and its exponent β is related to the local fractal dimension (FD) by:

$$FD = TD + 1 - \frac{\beta}{2}$$

¹⁴⁰ , where TD is the topological dimension in the Euclidean space of the fractional Brownian
¹⁴¹ motion. For one-dimensional fractional Brownian motion, TD = 1. The fractal dimension of
¹⁴² the two-dimensional surface $(FD)_2^*$ can be estimated as the average fractal dimension of the
¹⁴³ one-dimensional profiles $(FD)_1^*$:

$$(FD)_2^* = 1 + (FD)_1^*$$

¹⁴⁴ Users can specify the size (number of grids along each edge) of the moving window to study
¹⁴⁵ fractal characteristics at desired spatial scales. In addition to calculating the fractal dimension,
¹⁴⁶ the **pyfractd.py** module also computes reliability parameters such as standard error and the
¹⁴⁷ coefficient of determination (R^2) to assess the robustness of the analysis (Figure 2)[Figure 2](#).

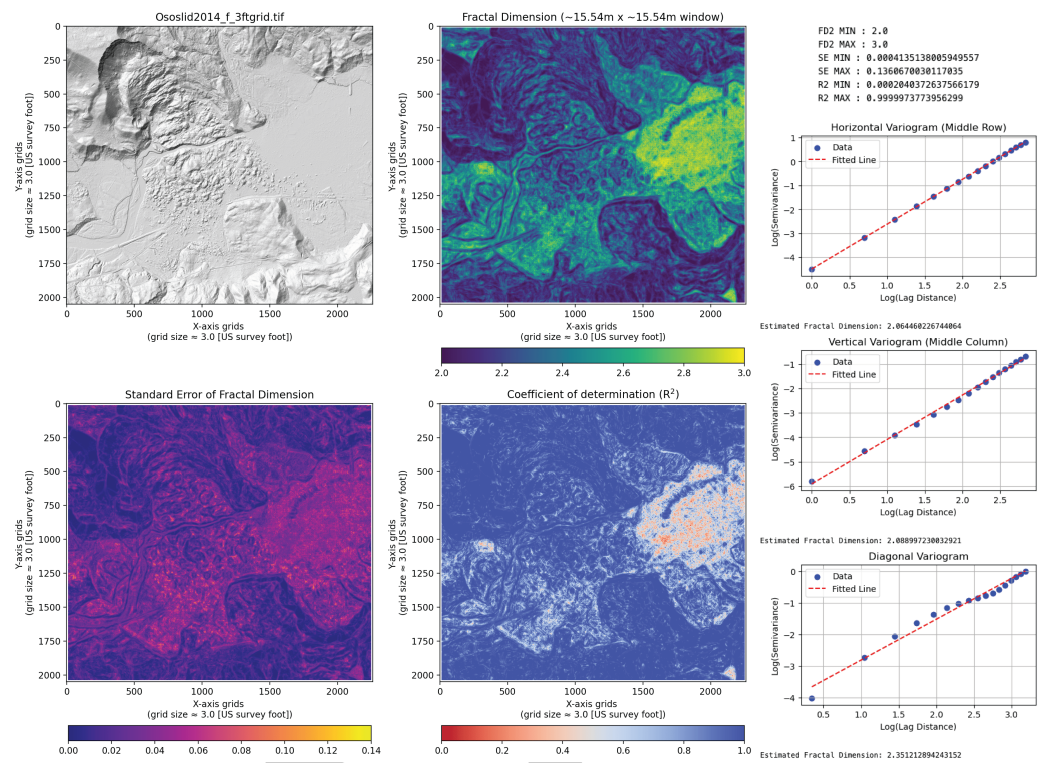


Figure 2: Figure 2. Hillshade map of the 2014 Oso Landslide region (upper-left), example variograms (right), and the results of Fractal Dimension (FD) analysis using the `pyfracd.py` module. The analysis was conducted with a designated 17 by 17 grid moving window size (grid spacing = 3 U.S. survey feet 0.9144 meters).

148 Rugosity Index calculation

149 The `pyrugosity.py` module in `pyTopoComplexity` measures the Rugosity Index of the land
150 surface, which is widely used to assess structural complexity of topography and has been
151 applied in classifying seafloor types by marine geologists and geomorphologists, understanding
152 small-scale hydrodynamics by oceanographers, and studying available habitats in the landscape
153 by ecologists and coral biologists (Emily R. Lundblad & Battista, 2006; Wilson et al., 2007).

154 The Rugosity Index is determined as the ratio of the contoured area (i.e., true geometric surface
155 area) to the planimetric area within the square moving window, highlighting smaller-scale
156 variations in surface height:

$$\text{Rugosity Index} = \frac{\text{Contoured area}}{\text{Planimetric area}}$$

157 This module adapts the Triangulated Irregular Networks method from Jenness (2004) to
158 approximate the contoured area as the sum of eight truncated-triangle areas. These triangles
159 connect the central grid point, four corner grid points, and four grid points at the middle
160 points of the surrounding edges within the moving window. If no local slope correction is
161 applied, the planimetric area is considered to be the horizontal planar area of the moving
162 window, as described in Jenness (2004). Another approach considers slope correction where to
163 the planimetric area is projected onto a plane of the local gradient (Du Preez, 2015).

164 By definition, the Rugosity Index has a minimum value of one (completely flat surface). Typical
165 values of the conventional rugosity index (without slope correction) range from one to three
166 although larger values are possible in very steep terrains. The slope-corrected rugosity index,

¹⁶⁷ also called arc-chord ratio (ACR) Rugosity Index, could provide a better representation of local
¹⁶⁸ surface complexity because it is not biased by slope (Figure 3)[Figure 3](#).

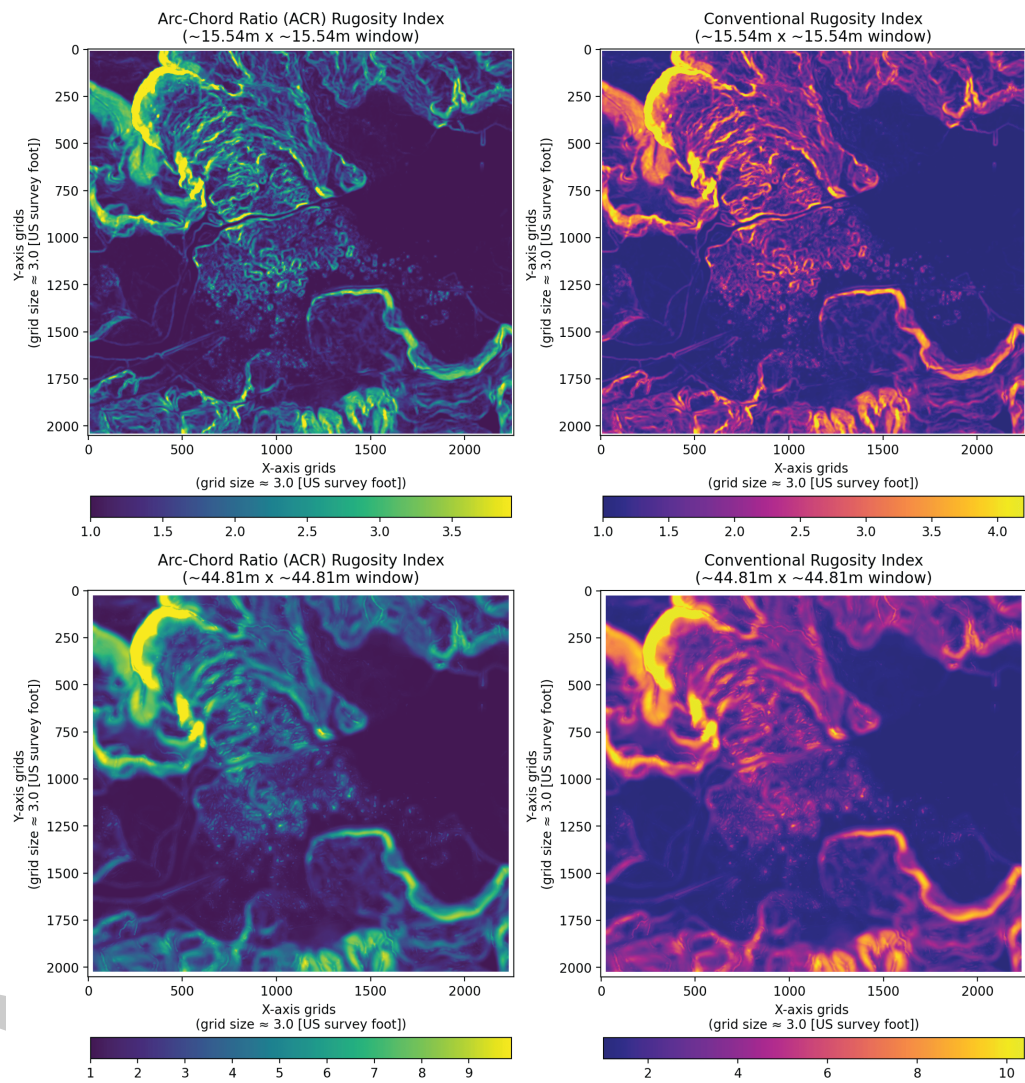


Figure 3: Figure 3. Calculated results of the Arc-Chord Ratio Rugosity Index (left) and the conventional Rugosity Index (right) for the 2014 Oso Landslide region, using the `pyrugosity.py` module. The calculations were performed with different moving window sizes: 17 by 17 grids (top) and 49 by 49 grids (bottom). Grid spacing is 3 U.S. survey feet (approximately 0.9144 meters).

¹⁶⁹ Terrain Position Index calculation

¹⁷⁰ The `pytpi.py` module in `pyTopoComplexity` calculates the Terrain Position Index (TPI) of the
¹⁷¹ land surface. The TPI, also known as the Topographic Position Index in terrestrial studies
¹⁷² ([Weiss, 2001](#)), measures the relative topographic elevation of a point compared to those of
¹⁷³ its surrounding landforms. This metric highlights regions relatively higher or lower than their
¹⁷⁴ surroundings, which is useful for distinguishing landscape features such as hilltops, valleys, flat
¹⁷⁵ plains, and slopes. In oceanography, an equivalent metric is the Bathymetric Position Index
¹⁷⁶ (BPI), which applies the TPI algorithm to bathymetric data to evaluate seafloor complexity.

¹⁷⁷ TPI is widely applicable for various purposes, including determining surface ruggedness ([Newman](#)
¹⁷⁸ et al., 2018), classifying terrain ([Zwoliński & Stefańska, 2015](#)), assessing local soil formation

179 and hydrodynamics (Deumlich et al., 2010; Liu et al., 2011), and identifying habitat hotspots
180 (Wilson et al., 2007). It is calculated by comparing the elevation of a grid cell (Z_{grid}) to the
181 mean elevation of its surrounding grid cells ($Z_{\text{neighborhood}}$) within a specified neighborhood:

$$\text{TPI} = Z_{\text{grid}} - \text{mean}(Z_{\text{neighborhood}})$$

182 In this module, the TPI is calculated for the central grid within a square moving window. Users
183 can specify the size of the window (i.e., the number of grids along each edge) to evaluate
184 topographic positions at various spatial scales. Positive TPI values indicate generally convex,
185 elevated features (e.g., ridges), while negative values represent concave depressions (e.g.,
186 valleys, saddles). Values close to zero denote relatively flat surface or area with near continuous
187 slope. The `pytpi.py` module also returns the absolute values of the TPI (Figure 4|Figure 4).
188 This absolute TPI calculation is suggested to be effective for quick assessments in mapping
189 and relative dating of deep-seated landslide deposits using high-resolution DTM data (Lai et
190 al., 2023).

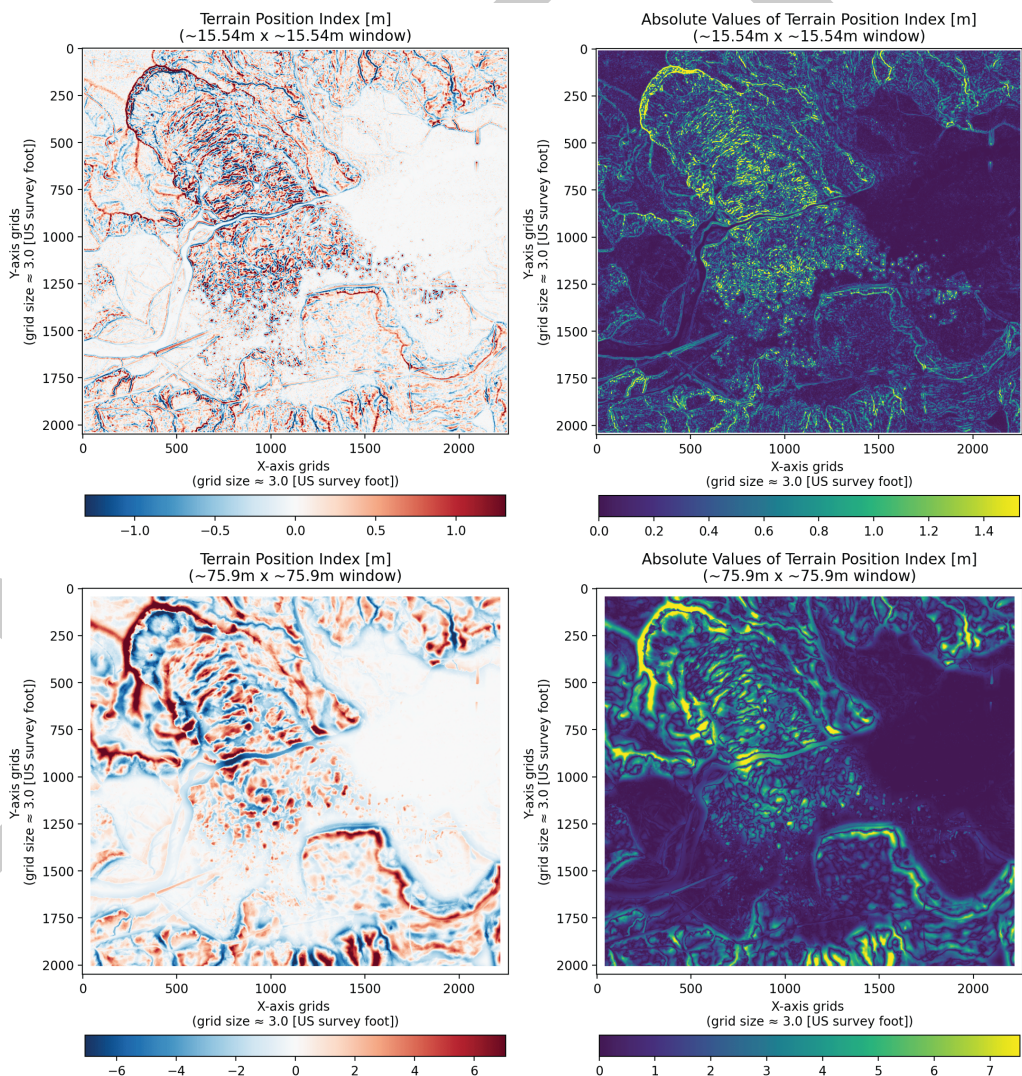


Figure 4: Figure 4. Calculated results of the Terrain Position Index (left) and its absolute values (right) for the 2014 Oso Landslide region, using the `pytpi.py` module. The calculations were performed with different moving window sizes: 17 by 17 grids (top) and 83 by 83 grids (bottom). Grid spacing is 3 U.S. survey feet (approximately 0.9144 meters).

191 **Forward simulation of landscape smoothing through nonlinear hillslope diffusion**
192 **processes**

193 The [nonlineardiff_Landlab.ipynb](#) notebook in the **pyTopoComplexity** package offers a sophis-
194 ticated tool for simulating landscape evolution through nonlinear diffusion processes due to
195 near-surface soil disturbances and downslope sediment creep ([Roering et al., 1999](#)). This tool
196 runs the simulation in the **Landlab** environment (version ≥ 2.7) ([Hobley et al., 2017](#)) with
197 the `TaylorNonLinearDiffuser` module from the `terrainBento` Python package ([Barnhart et](#)
198 [al., 2019](#)). The main simulation iteratively applies the nonlinear diffusion model to predict
199 changes in surface elevation z over time t :

$$\frac{\partial z}{\partial t} = -\nabla \cdot \mathbf{q}_s$$

200 , where (\mathbf{q}_s) represents the sediment flux at the surface. The sediment flux is further defined
201 by a nonlinear flux law ([Roering et al., 1999](#)) that is approximated using a Taylor series
202 expansion ([Ganti et al., 2012](#)):

$$\mathbf{q}_s = K \mathbf{S} \left[1 + \sum_{i=1}^N \left(\frac{S}{S_c} \right)^{2i} \right]$$

203 Here, $\mathbf{S} = -\nabla z$ represents the downslope topographic gradient, and S is its magnitude. S_c is
204 the critical slope representing the asymptotic maximum hillslope gradient. The parameter K is
205 a diffusion-like transport coefficient with dimensions of length squared per time. N denotes
206 the number of terms in the Taylor expansion, while i specifies the number of additional terms
207 included. If $N = 0$, the expression simplifies to linear diffusion ([Culling, 1963](#)). By default, N
208 is set to 2, that gives the behavior described in Ganti et al. ([2012](#)).

209 This notebook provides a comprehensive workflow that guides users through setting up,
210 importing raster files, and running simulations. Since **Landlab** primarily handles DTM data in
211 ESRI ASCII format, this notebook includes utility functions for converting raster files between
212 GeoTIFF and ESRI ASCII formats. Users are required to specify the values for S_c , K , the
213 length of each time step in years, and the final time to stop the simulation. The example
214 included in the notebook uses lidar DTM data from the 2014 Oso Landslide ([Washington](#)
215 [Geological Survey, 2023](#)), with parameter values provided in Booth et al. ([2017](#)), in an attempt
216 to reproduce the simulation results presented in that study (Figure 5[Figure 5](#)).

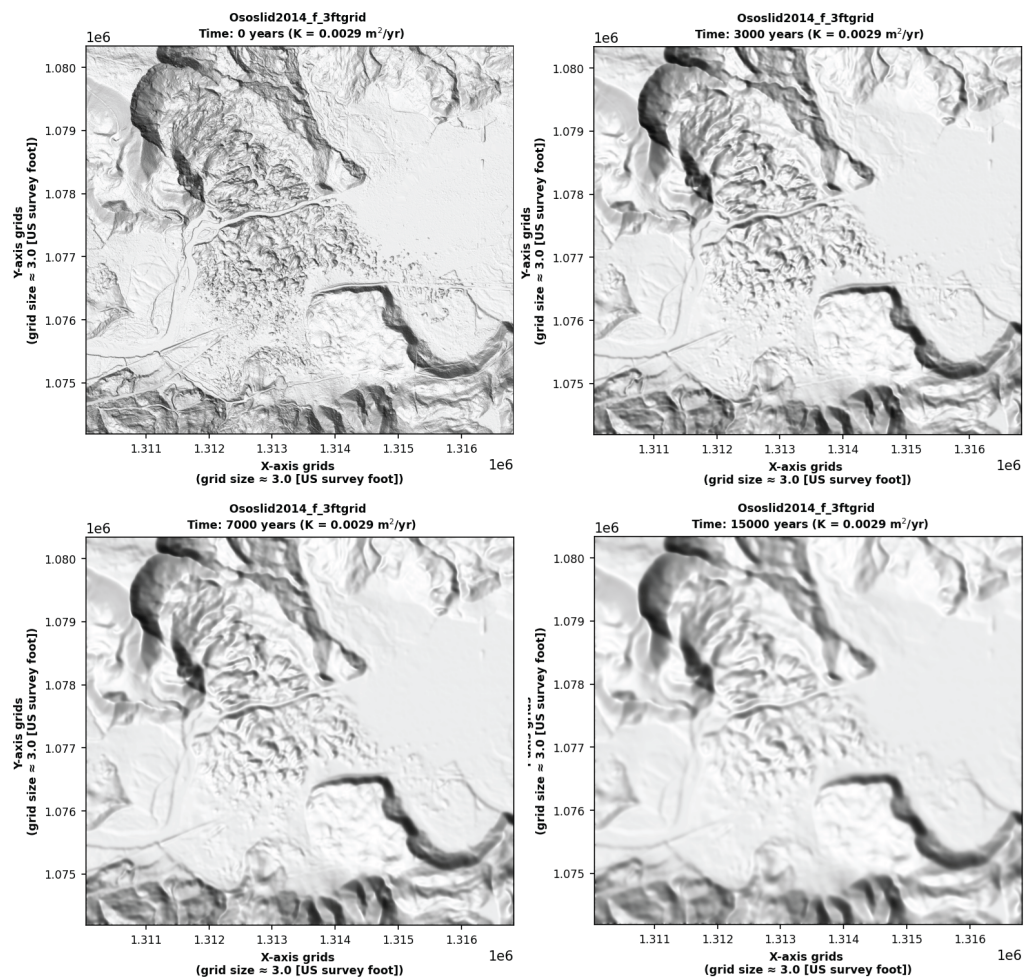


Figure 5: Figure 5. Hillshade maps of the 2014 Oso Landslide region and surface smoothing evolution over 15,000 years predicted by a nonlinear hillslope diffusion model used in the [nonlineardiff_Landlab.ipynb](#) notebook, in attempt to reproduce the simulation results in Booth et al. (2017).

Acknowledgements

217 The development of **pyTopoComplexity** is part of a collaborative effort within the [Landslide](#)
 218 [subteam](#) of the [Cascadia Coastlines and Peoples Hazards Research Hub \(Cascadia CoPes Hub\)](#),
 219 funded by the National Science Foundation Award ([#2103713](#)). We also acknowledge earlier
 220 funding by the National Science Foundation to Booth ([#2000188](#)) and Duvall ([#1953710](#)).
 221 We extend special thanks to Dr. Eulogio Pardo-Igúzquiza, who generously shared his Fortran
 222 code for fractal dimension analysis used in his work ([Pardo-Igúzquiza & Dowd, 2022b](#)), which
 223 inspired the development of the **pyfracd.py** module.
 224

References

- 226 Barnhart, K. R., Glade, R. C., Shobe, C. M., & Tucker, G. E. (2019). Terrainbento 1.0: A
 227 python package for multi-model analysis in long-term drainage basin evolution. *Geoscientific
 228 Model Development*, 12(4), 1267–1297. <https://doi.org/10.5194/gmd-12-1267-2019>
- 229 Benham, D. [drk944]. (2022). Rugosity_calculator. In *GitHub repository*. GitHub. https://github.com/drk944/Rugosity_Calculator

- 231 Berti, M., Corsini, A., & Daehne, A. (2013). Comparative analysis of surface roughness
232 algorithms for the identification of active landslides [Journal Article]. *Geomorphology*, 182,
233 1–18. <https://doi.org/10.1016/j.geomorph.2012.10.022>
- 234 Booth, A. M., LaHusen, S. R., Duvall, A. R., & Montgomery, D. R. (2017). Holocene
235 history of deep-seated landsliding in the north fork stillaguamish river valley from surface
236 roughness analysis, radiocarbon dating, and numerical landscape evolution modeling.
237 *Journal of Geophysical Research: Earth Surface*, 122(2), 456–472. <https://doi.org/10.1002/2016JF003934>
- 238
- 239 Booth, A. M., & Pétursson, H. G. (2023). *Permafrost controls on holocene bedrock landslides
in northern iceland*. Abstract (EP13C-1788) presented at 2023 AGU Fall Meeting, San
240 Francisco, CA. <https://agu.confex.com/agu/fm23/meetingapp.cgi/Paper/1256344>
- 241
- 242 Booth, A. M., Roering, J. J., & Perron, J. T. (2009). Automated landslide mapping using
243 spectral analysis and high-resolution topographic data: Puget sound lowlands, washington,
244 and portland hills, oregon. *Geomorphology*, 109(3-4), 132–147. <https://doi.org/10.1016/j.geomorph.2009.02.027>
- 245
- 246 Culling, W. E. H. (1963). Soil creep and the development of hillside slopes. *The Journal of
247 Geology*, 71(2), 127–161. <https://doi.org/10.1086/626891>
- 248 Deumlich, D., Schmidt, R., & Sommer, M. (2010). A multiscale soil–landform relationship in
249 the glacial-drift area based on digital terrain analysis and soil attributes. *Journal of Plant
250 Nutrition and Soil Science*, 173(6), 843–851. <https://doi.org/10.1002/jpln.200900094>
- 251 Dietrich, W. E., & Perron, J. T. (2006). The search for a topographic signature of life [Journal
252 Article]. *Nature*, 439(7075), 411–418. <https://doi.org/10.1038/nature04452>
- 253 Du Preez, C. (2015). A new arc–chord ratio (ACR) rugosity index for quantifying three-
254 dimensional landscape structural complexity [Journal Article]. *Landscape Ecology*, 30(1),
255 181–192. <https://doi.org/10.1007/s10980-014-0118-8>
- 256 Dubuc, B., Zucker, S. W., Tricot, C., Quiniou, J. F., Wehbi, D., & Berry, M. V. (1989).
257 Evaluating the fractal dimension of surfaces. *Proceedings of the Royal Society of London.
A. Mathematical and Physical Sciences*, 425(1868), 113–127. <https://doi.org/10.1098/rspa.1989.0101>
- 258
- 259
- 260 Emily R. Lundblad, J. M., Dawn J. Wright, & Battista, T. (2006). A benthic terrain
261 classification scheme for american samoa. *Marine Geodesy*, 29(2), 89–111. <https://doi.org/10.1080/01490410600738021>
- 261
- 262
- 263 Frost, N. J., Burrows, M. T., Johnson, M. P., Hanley, M. E., & Hawkins, S. J. (2005). Measuring
264 surface complexity in ecological studies [Journal Article]. *Limnology and Oceanography:
265 Methods*, 3(4), 203–210. <https://doi.org/10.4319/lom.2005.3.203>
- 266
- 267 Ganti, V., Passalacqua, P., & Foufoula-Georgiou, E. (2012). A sub-grid scale closure for
268 nonlinear hillslope sediment transport models. *Journal of Geophysical Research: Earth
Surface*, 117(F2). <https://doi.org/10.1029/2011jf002181>
- 269
- 270 Glenn, N. F., Streutker, D. R., Chadwick, D. J., Thackray, G. D., & Dorsch, S. J. (2006).
271 Analysis of LiDAR-derived topographic information for characterizing and differentiating
272 landslide morphology and activity [Journal Article]. *Geomorphology*, 73(1), 131–148.
<https://doi.org/10.1016/j.geomorph.2005.07.006>
- 273
- 274 GRASS Development Team. (2023). *Geographic resources analysis support system (GRASS
GIS) software, version 8.2*. Open Source Geospatial Foundation. <https://doi.org/10.5281/zenodo.5176030>
- 275
- 276 Herzig, E. N., Duvall, A. R., Booth, A. R., Stone, I., Wirth, E., LaHusen, S. R., Wartman, J.,
277 & Grant, A. (2023). Evidence of seattle fault earthquakes from patterns in deep-seated
278 landslides. *Bulletin of the Seismological Society of America*. <https://doi.org/10.1785/>

279 0120230079

- 280 Hetz, G., Mushkin, A., Blumberg, D. G., Baer, G., & Ginat, H. (2016). Estimating the age of
281 desert alluvial surfaces with spaceborne radar data [Journal Article]. *Remote Sensing of
282 Environment*, 184, 288–301. <https://doi.org/10.1016/j.rse.2016.07.006>
- 283 Hobley, D. E. J., Adams, J. M., Nudurupati, S. S., Hutton, E. W. H., Gasparini, N. M.,
284 Istanbulluoglu, E., & Tucker, G. E. (2017). Creative computing with landlab: An open-
285 source toolkit for building, coupling, and exploring two-dimensional numerical models of
286 earth-surface dynamics. *Earth Surface Dynamics*, 5, 21–46. <https://doi.org/10.5194/esurf-5-21-2017>
- 288 Jenness, J. S. (2004). Calculating landscape surface area from digital elevation models. *Wildlife
289 Society Bulletin*, 32(3), 829–839. [https://doi.org/10.2193/0091-7648\(2004\)032%5B0829:CLSAFD%5D2.0.CO;2](https://doi.org/10.2193/0091-7648(2004)032%5B0829:CLSAFD%5D2.0.CO;2)
- 291 Johnstone, S. A., Hudson, A. M., Nicovich, S., Ruleman, C. A., Sare, R. M., & Thompson,
292 R. A. (2018). Establishing chronologies for alluvial-fan sequences with analysis of high-
293 resolution topographic data: San Luis Valley, Colorado, USA. *Geosphere*, 14(6), 2487–2504.
294 <https://doi.org/10.1130/GES01680.1>
- 295 LaHusen, S. R., Duvall, A. R., Booth, A. M., Grant, A., Mishkin, B. A., Montgomery, D. R.,
296 Struble, W., Roering, J. J., & Wartman, J. (2020). Rainfall triggers more deep-seated
297 landslides than cascadia earthquakes in the oregon coast range, USA. *Science Advances*,
298 6(38), eaba6790. <https://doi.org/10.1126/sciadv.aba6790>
- 299 Lai, L. S.-H., Duvall, A. R., Booth, A. M., Wartman, J., Grant, A. R. R., & LaHusen, S.
300 R. (2023). Preliminary mapping of deep-seated landslides in the washington coast range,
301 cascadia subduction zone. Abstract (EP23D-1963) presented at 2023 AGU Fall Meeting,
302 San Francisco, CA. <https://agu.confex.com/agu/fm23/meetingapp.cgi/Paper/1270349>
- 303 Lashermes, B., Foufoula-Georgiou, E., & Dietrich, W. E. (2007). Channel network extraction
304 from high resolution topography using wavelets. *Geophysical Research Letters*, 34(23).
305 <https://doi.org/10.1029/2007GL031140>
- 306 Lindsay, J. B. (2016). Whitebox GAT: A case study in geomorphometric analysis [Journal
307 Article]. *Computers & Geosciences*, 95, 75–84. <https://doi.org/10.1016/j.cageo.2016.07.003>
- 309 Lindsay, John B., Newman, D. R., & Francioni, A. (2019). Scale-optimized surface roughness
310 for topographic analysis [Journal Article]. *Geosciences*, 9(7), 322. <https://doi.org/10.3390/geosciences9070322>
- 312 Liu, H., Bu, R., Liu, J., Leng, W., Hu, Y., Yang, L., & Liu, H. (2011). Predicting the wetland
313 distributions under climate warming in the great xing'an mountains, northeastern china.
314 *Ecological Research*, 26(3), 605–613. <https://doi.org/10.1007/s11284-011-0819-2>
- 315 Malamud, B. D., & Turcotte, D. L. (2001). Wavelet analyses of mars polar topography.
316 *Journal of Geophysical Research: Planets*, 106(E8), 17497–17504. <https://doi.org/10.1029/2000JE001333>
- 318 Mandelbrot, B. B., & Wheeler, J. A. (1983). The fractal geometry of nature. *American
319 Journal of Physics*, 51(3), 286–287. <https://doi.org/10.1119/1.13295>
- 320 Newman, D. R., Lindsay, J. B., & Cockburn, J. M. H. (2018). Evaluating metrics of local
321 topographic position for multiscale geomorphometric analysis. *Geomorphology*, 312, 40–50.
322 <https://doi.org/10.1016/j.geomorph.2018.04.003>
- 323 Ozioko, O., Booth, A. M., & Duvall, A. R. (2023). Temporal clustering of deep-seated landslides
324 in the puget lowlands: A seismic trigger? Abstract (EP23D-1967) presented at 2023 AGU
325 Fall Meeting, San Francisco, CA. <https://agu.confex.com/agu/fm23/meetingapp.cgi/Paper/1336351>

- 327 Pardo-Igúzquiza, E., & Dowd, P. A. (2020). Fractal analysis of karst landscapes [Journal Article].
328 *Mathematical Geosciences*, 52(4), 543–563. <https://doi.org/10.1007/s11004-019-09803-x>
- 329 Pardo-Igúzquiza, E., & Dowd, P. A. (2022a). Fractal analysis of the martian landscape: A
330 study of kilometre-scale topographic roughness [Journal Article]. *Icarus*, 372, 114727.
331 <https://doi.org/10.1016/j.icarus.2021.114727>
- 332 Pardo-Igúzquiza, E., & Dowd, P. A. (2022b). The roughness of martian topography: A
333 metre-scale fractal analysis of six selected areas. *Icarus*, 384, 115109. <https://doi.org/10.1016/j.icarus.2022.115109>
- 335 QGIS Development Team. (2023). *QGIS geographic information system*. QGIS Association.
336 <https://www.qgis.org>
- 337 Ricker, N. (1943). Further developments in the wavelet theory of seismogram structure*.
338 *Bulletin of the Seismological Society of America*, 33(3), 197–228. <https://doi.org/10.1785/BSSA0330030197>
- 340 Robbins, S. J. (2018). The fractal nature of planetary landforms and implications to geologic
341 mapping. *Earth and Space Science*, 5(5), 211–220. <https://doi.org/10.1002/2018EA000372>
- 343 Roering, J. J., Kirchner, J. W., & Dietrich, W. E. (1999). Evidence for nonlinear, diffusive sediment
344 transport on hillslopes and implications for landscape morphology. *Water Resources Research*, 35(3), 853–870. <https://doi.org/10.1029/1998wr900090>
- 346 Struble, W. T., Roering, J. J., Dorsey, R. J., & Bendick, R. (2021). Characteristic scales of
347 drainage reorganization in cascadia. *Geophysical Research Letters*, 48(3), e2020GL091413.
348 <https://doi.org/10.1029/2020GL091413>
- 349 Taud, H., & Parrot, J.-F. (2005). Measurement of DEM roughness using the local fractal
350 dimension. *Géomorphologie: Relief, Processus, Environnement*, 11(4), 327–338. <https://doi.org/10.4000/geomorphologie.622>
- 352 Torrence, C., & Compo, G. P. (1998). A practical guide to wavelet analysis. *Bulletin of the American Meteorological Society*, 79(1), 61–78.
- 354 Underwood, A. C. (2022). *Most recent rupture on the boulder creek fault triggered bedrock landsliding in the nooksack watershed, whatcom county, washington* [Thesis]. <https://doi.org/10.15760/etd.8130>
- 357 Virtanen, P., Gommers, R., Oliphant, T. E., Haberland, M., Reddy, T., Cournapeau, D.,
358 Burovski, E., Peterson, P., Weckesser, W., Bright, J., van der Walt, S. J., Brett, M., Wilson,
359 J., Millman, K. J., Mayorov, N., Nelson, A. R. J., Jones, E., Kern, R., Larson, E., ... SciPy
360 1.0 Contributors. (2020). SciPy 1.0: Fundamental Algorithms for Scientific Computing in
361 Python. *Nature Methods*, 17, 261–272. <https://doi.org/10.1038/s41592-019-0686-2>
- 362 Walbridge, S., Slocum, N., Pobuda, M., & Wright, D. J. (2018). Unified geomorphological
363 analysis workflows with benthic terrain modeler. *Geosciences*, 8(3). <https://doi.org/10.3390/geosciences8030094>
- 365 Washington Geological Survey. (2023). *'Stillaguamish 2014' project [lidar data], originally
366 contracted by washington state department of transportation (WSDOT)*. Accessed april 4,
367 2024, at <http://lidarportal.dnr.wa.gov>.
- 368 Weiss, A. (2001). Topographic position and landforms analysis. *Poster Presentation, ESRI
369 User Conference, San Diego, CA, 200*.
- 370 Wen, R., & Sinding-Larsen, R. (1997). Uncertainty in fractal dimension estimated from
371 power spectra and variograms [Journal Article]. *Mathematical Geology*, 29(6), 727–753.
372 <https://doi.org/10.1007/BF02768900>
- 373 Wilson, M. F. J., O'Connell, B., Brown, C., Guinan, J. C., & Grehan, A. J. (2007). Multiscale

- 374 terrain analysis of multibeam bathymetry data for habitat mapping on the continental
375 slope. *Marine Geodesy*, 30(1-2), 3–35. <https://doi.org/10.1080/01490410701295962>
- 376 Xu, T., Moore, I. D., & Gallant, J. C. (1993). Fractals, fractal dimensions and landscapes — a
377 review. *Geomorphology*, 8(4), 245–262. [https://doi.org/10.1016/0169-555X\(93\)90022-T](https://doi.org/10.1016/0169-555X(93)90022-T)
- 378 Zwoliński, Z., & Stefańska, E. (2015). Relevance of moving window size in landform classifica-
379 tion by TPI. In J. Jasiewicz, Z. Zwoliński, H. Mitasova, & T. Hengl (Eds.), *Geomorphometry*
380 for geosciences (pp. 273–277). Bogucki Wydawnictwo Naukowe. ISBN: 978-83-7986-059-3

DRAFT